Mecánica Computacional Vol. XXIV
A. Larreteguy (Editor)
Buenos Aires, Argentina, Noviembre 2005

THE MODELING OF AIR ENTRAINMENT PROCESSES FOR SURFACE SHIPS.

Francisco J. Moraga*, Pablo M. Carrica†, Donald A. Drew*and Richard T. Lahey, Jr.*

*Center for Multiphase Research
Rensselaer Polytechnic Institute,
Troy, New York 12180-3590. USA.
e-mail: moragf2@rpi.edu

†Iowa Institute of Hydraulic Research
The University of Iowa,
Iowa City, Iowa 52242-1585. USA.
e-mail: pcarrica@engineering.uiowa.edu

Key Words: air entrainment, two-fluid model, bubbly flow, breaking waves, ship hydrodynamics, turbulence modeling.

Abstract. *Direct numerical simulations (DNS) of air entrainment by breaking bow waves of naval surface ships are outside of the computational reach of the most powerful computers in the foreseeable future. This creates a need for models of air entrainment for applications in numerical simulations for ship design. We present a model that is based on the local liquid velocity and the distance to the interface, which determines whether air entrainment should occur. Using this model and the bubble size distributions measured by Deane and Stokes*[1] *we simulate the air entrainment in the breaking bow wave experiments of Wanieski et al.*[2] *Comparison against these experimental data is good. We then apply this model to simulate the flow around naval combatant DTMB5415. The model predicts air entrainment in all the regions where it is actually observed at sea, namely the breaking bow wave, along the water/air/hull contact line and around the transom stern. To the best of our knowledge this is the first model of air entrainment that compares favorably with data at laboratory scale and presents the right trends at full-scale conditions.*

1 INTRODUCTION

The simulation of air entrainment flows is of interest in ship hydrodynamics due to its implication for stealth capabilities, drag reduction and general design purposes. It is not only desirable to know where the bubbles are produced but also how their presence affects the flow fields that are normally calculated neglecting the presence of the bubbles, although very high void fractions (i.e., 10 % or higher) are to be expected in some regions of the flow. Air entrainment is also of importance for the design of spillways, hydraulic jumps and other facilities designed by civil engineers.[3] Finally the formation of air bubbles by ambient oceanic breaking waves plays an important role in the exchange of gases between the ocean and the atmosphere.

In all these applications very large numbers of bubbles are formed, the air/water interface is highly unstable and its length scales range from those dominated by surface tension and turbulence (typically in the order of microns) to those of the mean flow (typically with length scales of the order ofseveral meters). Given these features it is not surprising that few researchers have tried to conduct Direct Numerical Simulations (DNS) of flows with air entrainment. Due to its agreement with the macroscopic features of experimental data the work of Iafrati et al[4] is particularly significant. These authors used a level set technique to simulate the air entrainment by a two-dimensional plunging liquid jet in a grid of approximately one million cells. They had to stop the simulation immediately after the formation of the first air cavity due to lack of spatial resolution and were unable to capture the formation of the multitude of small bubbles around the main air cavity, again presumably due to lack of sufficient spatial resolution. Since we are interested in continuing the simulation until the main air cavity has broken up and a statistical equilibrium in the bubble population has been achieved, it is to be expected that a considerably higher spatial resolution than that used by Iafrati et al is needed. It should be noted that the successful capture of the macroscopic features of the interface for the 3D flow around a ship model for tow tank conditions requires of the order of two million cells.[5] Obviously this number would increase dramatically if the grid is refined sufficiently to resolve the formation of air bubbles. Based on these arguments we believe that the DNS simulation of air entrainment flows will remain so computationally expensive that its main use will be as a tool to develop subgrid models of air entrainment process.

The main objective of this paper is to present a subgrid model that detects the location of the air bubble entrainment region. Here our use of the term “subgrid” implies that the model is designed to work in grids that do not have sufficient spatial resolution as to capture the details of the air entrainment process. Rather, it has to be modeled. In this sense the situation is completely analogous to that of turbulence modeling in which Reynolds Averaged Navier Stokes (RANS) models are often used when there is not sufficient spatial and temporal resolution to capture all the flow features. In our case the grid will be insufficient to resolve the free surface at the scales of the bubble formation. Yet if the description of the problem in terms of the free surface location, average fluid velocities, turbulent kinetic energy and turbulent dissipation carries enough information to detect the location of the bubble source such that a subgrid model for the determination of the air entrainment region should be possible. In this work we show that using a subgrid model for the location of the bubble source it is possible to obtain reasonable quantitative agreement with the measurements of air entrainment by bow waves conducted by Wanieski et al.[2] Moreover, the model properly identifies the location of all the bubble sources in the flow around a naval surface ship. Although no quantitative data are available in the open literature for the air entrainment around ship flows, there is an abundance of qualitative data.

Once the location of the air entrainment region has been calculated using our subgrid model, a two-fluid model can be used to compute the transport of the bubbles. Due to the need for specifying a bubble size distribution and a source intensity (i.e., the number of bubbles entrained per unit time and per unit volume generated by the air entrainment) at the source location our simulations have not reached a completely predictive stage. However, our subgrid model greatly advances the state-of-the-art of two-fluid model simulations of the flow around surface ships in which not only the bubble size distribution and source intensity but also the source location is an input for the simulation instead of being part of the computational results. For more description of the current state-of-the art of the source specification for two-fluid model simulations of the flow around ships see the work of Moraga et al[6,7] and Carrica et al. [8]

High void fractions and strong turbulence-induced breakup are expected in the air entrainment region.[1] This fact calls for a two-fluid model that can handle polydisperse bubble populations, two-way coupling and turbulence-induced bubble breakup in close proximity to a free surface. Although other researchers have developed two-fluid models with some of these features,[9] we are not aware of any implementation of a two-fluid model that combines all of them in a single implementation.

2 TWO-FLUID MODEL

2.1 Mass conservation of the dispersed phase

To simulate polydisperse flows we separate the bubbles of different sizes into G classes, or groups, having a characteristic equivalent bubble diameter of $D_g; g = 1, 2, ..G$. In absence of bubble coalescence and dissolution the conservation equation for the bubble number density, N_g''', for bubbles of characteristic diameter, D_g moving with velocity $\mathbf{u}_g$, can be derived from a Boltzmann-type transport equation, often referred to as the population balance equation:[10,11]

$$\frac{\partial\, N_g'''}{\partial\, t} + \nabla \cdot \left(\mathbf{u}_g\, N_g'''\right) = \mathcal{E}_g + \mathcal{B}_g^{+} - \mathcal{B}_g^{-}, \tag{1}$$

where $\mathcal{E}_g$ is the source of bubbles due to air ingestion and is one of the main focuses of this work. The other sources/sinks of bubbles on the right hand side of equation (1) are due to bubble breakup.

2.1.1 The bubble source due to air entrainment

We model this source as,

$$\mathcal{E}_g(\mathbf{x}) = S_0 f_E(D_g) \Delta D_g \sum_s \delta(\mathbf{x} - \mathbf{x}_s), \tag{2}$$

where S_0 is a constant that determines the bubble source intensity, $f_E(D_g)$ is a bubble size probability density function and ΔD_g is the width of the bin with characteristic diameter D_g. The sum over the Dirac delta function, $\delta(\mathbf{x} - \mathbf{x}_s)$, is used to selectively activate the source at the chosen points, $\mathbf{x_s}$, within the liquid region. Notice that in reality, air entrainment is an interfacial process. We have two options to model the air entrainment, namely a boundary condition at the interface or a volumetric source in a region close to the interface. Since we do not resolve the small scales necessary to predict bubble entrainment, applying a boundary condition to simulate the air entrainment process is problematic because bubbles are entrained in short transient localized processes which are difficult, if not impossible, to simulate with a RANS approach. The volumetric source, on the other hand, account for the fact that once the bubbles are entrained, they'll behave as a standard multiphase flow that obeys to the two-fluid model approach that we follow.

Deane & Stokes[1] measured the bubble size spectrum in breaking waves and found that,

$$f_E(D_g) = \left\{ \begin{array}{ll} (D_g/2)^{\alpha} & \text{if } D_g/2 < 1mm \\ (D_g/2)^{\beta} & \text{if } D_g/2 > 1mm \end{array} \right. . \tag{3}$$

where the constant exponents α and β depend on the age of the bubbly plume. Deane and Stokes divide the lifetime of the bubbly plume into two phases; the acoustic phase where bubbles are born and the quiescent phase which begins when active bubble formation ceases. The name of the acoustic phase is derived form the fact that bubble formation is accompanied by the emission of audible noise. It is the short lived acoustic phase that determines the initial bubble size distribution, while its evolution in the quiescent plume phase is controlled by advection, turbulent transport and buoyancy. Since our two-fluid model is able to account for all these phenomena, we are interested in the size distribution at the end of the acoustic phase. In other words, our subgrid model of air entrainment by design aims at modeling the acoustic phase with dealing with all the physics of bubble formation. This is made possible by the fact that the time scale of the acoustic phase is at least one order of magnitude shorter than that of the quiescent phase. We also notice that most measurements of bubble size distribution below breaking waves are for the quiescent phase and consequently they are less suitable to our purposes than the measurements of Deane & Stokes. The exponents measured by Deane and Stokes for the acoustic phase are $\alpha = -3/2$ and $\beta = -10/3$.

Before describing how we select the points, $\mathbf{x_s}$, where bubbles are injected, it is worth giving a short description of the physical phenomena we aim to capture. Practically all air entrainment flows are characterized by a region of very high void fraction below the interface separating the continuous fluids. At the edge of this region the void fraction falls abruptly. See for examples the photographs in Figure 2 in the work of Deane & Stokes[1] or Figure-1 of Clanet et al.[12] As Clanet et al[12] point out, this abrupt change of the void fraction is due to the fact that the terminal velocity of bubbles is not a monotonous function of the bubble diameter, but presents a minimum at about 0.22 m/s, independently of the Morton number of the bubbles.[13] All bubbles of diameter larger than a critical diameter, D_{bc}, have terminal velocities larger than 0.22 m/s, and in the case of water, $D_{bc} \approx 1$ mm. As a consequence, at the surface where the continuous liquid is moving downward at the velocity 0.22 m/s there has to be an abrupt change of void fraction, because only the small bubbles of diameter $D_b < D_{bc}$ can cross this surface. All other bubbles will start to rise before or when they reach this surface. This idea is so robust that Clanet et al[12] successfully used it to predict the functional dependence of the penetration depth of bubbles in plunging liquid jets as a function of the jet diameter, velocity and incidence angle. Our subgrid model of air entrainment aims at identifying the localized region of high void fraction bounded by the surface at which the downward liquid velocity is 0.22 m/s at the place where bubbles are originated. This is the volume where bubbles are formed either as a direct consequence of the liquid jet impact or from the breakup of larger bubbles. Consistent with these ideas, in our model the locations where air injection takes place, $\mathbf{x_s}$, satisfy the conditions,

$$0 < \phi(\mathbf{x_s}) < \phi_{ent} \tag{4}$$

and,

$$\mathbf{v}_c(\mathbf{x_s}) \cdot \frac{\mathbf{g}}{|\mathbf{g}|} > v_{ent} \approx 0.22 \ \text{ m/s} \tag{5}$$

where ϕ and $\mathbf{g}$ are the distance to the interface and the gravity vector, respectively. The model constant, ϕ_{ent}, was used to select a band below the free-surface where the bubble source can be non-zero and represents the maximum depth that bubbles can reach during the unresolved acoustic phase. The model constant, ϕ_{ent}, can be estimated from the depth of penetration of bubbles entrained by plunging liquid jets. Reliable correlations exist for this depth.[12] Moreover, in all flows such that the downward liquid velocity decreases monotonically with distance from the interface, there is no penalty for overestimating ϕ_{ent}, which eliminates one adjustable parameter. This is important because many air entrainment flows, plunging liquid jets among them, are characterized by monotonically decreasing downward velocities. In particular the steady breaking wave which we have simulated satisfy this condition. Thus in the breaking bow wave simulations presented below there is no need to adjust the parameter ϕ_{ent}. Only for complex flows, such as those of ship flows is it necessary to introduce the parameter ϕ_{ent} to ensure that no bubbles are ingested too far from the interface, but even in this situation this parameter has a clear physical interpretation. The other model constant, $v_{ent} \approx 0.22$ m/s, is not an adjustable parameter but is the terminal velocity at which there is a relative minimum in a terminal velocity vs. bubble diameter plot.[13] Thus, the only adjustable parameters in our model for the bubble source due to air entrainment, $\mathcal{E}_g$, are S_0 in equation (2), and for some flows, ϕ_{ent}.

2.1.2 The bubble source due to bubble breakup

The terms $\mathcal{B}_g^+$ and $\mathcal{B}_g^-$ in Equation (1) represent the net gain and loss, respectively, of bubbles of size D_g due to bubble breakup and are modeled using the turbulence-induced bubble breakup model of Martinez-Bazan et al,[10,14,15]

$$\mathcal{B}_g^+ = \int_{D_g}^{\infty} m(D_0) f(D_g, D_0) g(D_0) N_0''' dD_0 \tag{6}$$

and

$$\mathcal{B}_g^- = g(D_g) N_g'''. \tag{7}$$

The symbol $g(D_g)$ represents the bubble breakup frequency of bubbles of equivalent diameter D_g, $m(D_0)$ is the mean number of bubbles resulting from the breakup of a mother bubble of size D_0, and $f(D_g, D_0)$ is the size distribution of daughter bubbles formed from the breakage of a mother bubble of size D_0. Martinez-Bazan et al[10,14] give the breakup frequency and the probability density function of the daughter bubbles for binary breakup ($m(D_0) = 2$), as,

$$g(\epsilon, D_0) = K_g D_0^{-1} \sqrt{\beta \left(\epsilon D_0\right)^{2/3} - 12\sigma / \left(\rho D_0\right)} \tag{8}$$

and,

$$f(D^*) = \frac{\left[D^{*2/3} - \Lambda^{5/3}\right]\left[\left(1 - D^{*3}\right)^{2/9} - \Lambda^{5/3}\right]}{\int_{D^*_{min}}^{D^*_{max}} \left[D^{*2/3} - \Lambda^{5/3}\right]\left[\left(1 - D^{*3}\right)^{2/9} - \Lambda^{5/3}\right] dD^*} \tag{9}$$

where the model coefficients $K_g = 0.25$ and $\beta = 8.2$ were found experimentally[10,16] and the nondimensional critical bubble diameter is given by,

$$\Lambda = D_c/D_0 = \left(12\sigma / \left(\beta\rho\right)\right)^{3/5} \epsilon^{-2/5} D_0^{-1}. \tag{10}$$

The dimensionless daughter bubble diameter, $D^* = D/D_0$, ranges from a minimum value of, $D^*_{min} = \left(\frac{12\sigma}{\beta\rho}\right)^{3/2} \epsilon^{-1} D_0^{-5/2}$, to a maximum value of, $D^*_{max} = [1 - D^3_{min}/D^3_0]^{1/3}$. In the equations above, ϵ is the turbulent dissipation, σ the surface tension of the air/water system and ν is the kinematic viscosity of the liquid.

2.2 Momentum conservation of the dispersed phase

Conservation of the ensemble-averaged momentum equations for the bubble group of size D_g may be expressed as,[11,17]

$$\frac{\partial \overline{v_g} N_g''' \rho_d \mathbf{u}_g}{\partial t} + \nabla \cdot \overline{v_g} N_g''' \rho_d \mathbf{u}_g \mathbf{u}_g = \nabla \cdot \overline{v_g} N_g''' \left(\mathbf{T}_g + \mathbf{T}_g^{Re}\right) + \overline{v_g} N''' \rho_d \, \mathbf{g} + \mathbf{M}_g \,. \tag{11}$$

where $\overline{v_g}$ is the average volume of a bubble of diameter D_g. The interfacial force density, $\mathbf{M}_g$, the microscale tensor, $\mathbf{T}_g$, and, the Reynolds stress, $\mathbf{T}_g^{Re}$, for the dispersed phase need to be constituted to achieve closure. Based on the large density ratio between the phases in an air/water bubbly flow we neglect the Reynolds stress of the dispersed phase in the remainder of this work. We also neglect viscous shear stresses and assume that the pressure varies little in the interior of bubbles[18] and that the ensemble averaged pressure of both phases are approximately equal (i.e., $p_g \approx p_{gi} \approx p_c$, where the subindex i indicates interfacial magnitude). With these assumptions, which are routinely used for air/water bubbly flows,[17] equation (11) becomes,

$$\frac{\partial \overline{v_g} N_g''' \rho_d \mathbf{u}_g}{\partial t} + \nabla \cdot \overline{v_g} N_g''' \rho_d \mathbf{u}_g \mathbf{u}_g = \overline{v_g} N_g''' \nabla p_c + \overline{v_g} N''' \rho_d \, \mathbf{g} + \mathbf{M}_g' \, . \tag{12}$$

where the interfacial force density, $\mathbf{M}_g$ was split into two forces, one dependent on the mean field values and another, $\mathbf{M}_g'$, on the fluctuating values. The mean force is modeled taking into account only the mean pressure forces on the mean bubble, and neglecting viscous stresses. Because it is not the main focus of this work, we have moved the description of the closure for the fluctuating interfacial force density to Section 2.6.

2.3 Mass conservation of the continuous phase

The continuity equation for the liquid phase reads,[18]

$$\frac{\partial \alpha_c \rho_c}{\partial t} + \nabla \cdot \alpha_c \rho_c \mathbf{u}_c = 0 \tag{13}$$

It should be noted here that, although the liquid is assumed incompressible, the ensemble averaged liquid velocity, $\mathbf{u}_c$, has non-zero divergence if the void fraction varies in time or space. When no bubbles are present, $\alpha_c = 1$, and consequently Eq.(13) reduces to the mass conservation equation of an incompressible fluid. Given the geometrical restriction,

$$\alpha_c = 1 - \sum_{g=1}^{G} \alpha_g \tag{14}$$

the liquid volume fraction can be calculated after the void fractions α_g were related to the calculated number density N_g''' using equation(15), which is valid far away from walls,

$$\alpha_g(\mathbf{x}, t) = \overline{v_g} N^{\eta'''}. \tag{15}$$

where $\overline{v_g}$ is the mean bubble volume. The case of proximity to a wall was of little interest in this work, since the bubbles are all away from the wall. The interested reader is referred elsewhere.[17]

2.4 Momentum conservation of the continuous phase

Conservation of momentum for the continuous phase in the average sense is expressed as,[18]

$$\frac{\partial \alpha_c \rho_c \mathbf{u}_c}{\partial t} + \nabla \cdot \alpha_c \rho_c \mathbf{u}_c \mathbf{u}_c = \nabla \cdot \alpha_c (\mathbf{T}_c + \mathbf{T}_c^{Re}) + \alpha_c \rho_c \mathbf{g} + \mathbf{M}_c \, , \tag{16}$$

The reader interested in the modeling of the shear stress tensor, $\mathbf{T}_c$ is referred to the work of Larreteguy et al.[19] The Reynolds stress tensor is modeled as if it were a single-phase flow, that is,

$$\mathbf{T}_c^{Re} = -(\frac{2}{3}\rho_c k)\mathbf{I} + 2\mu_t \mathbf{D}_c \tag{17}$$

where $\mathbf{I}$ is the identity tensor, and we introduce the turbulence-induced pressure as,

$$p_{1\phi}^{Re} = \frac{2}{3}\rho_l k \ , \tag{18}$$

and the turbulence-induced shear stress as,

$$\tau_{1\phi}^{Re} = 2\mu_t \mathbf{D}_c = \mu_t \left[\nabla \mathbf{u}_c + (\nabla \mathbf{u}_c)^T\right] \ , \tag{19}$$

Here, $k = \frac{1}{2}\overline{\mathbf{u}' \cdot \mathbf{u}'}$ is the turbulent kinetic energy and μ_t is the so called turbulent viscosity. Finally, the interfacial force density, $\mathbf{M}_c$, of the continuous phase is related to that of the discrete phase by the interfacial jump condition,[18,19]

$$\mathbf{M}_c + \sum_{g=1}^{G} \mathbf{M}_g = \mathbf{m}_\sigma \tag{20}$$

where $\mathbf{m}_\sigma$ accounts for the interfacial surface tension contribution to the momentum jump. Our closure model for $\mathbf{m}_\sigma$ has been described elsewhere.[18,19] Here it suffices to mention that the contribution of $\mathbf{m}_\sigma$ is negligible in the simulations presented herein. This is consistent with the work of other researchers that found good agreement with experimental data for bubbly flows by setting $\mathbf{m}_\sigma = 0$.[9] It is clear from equations (16) and (20) that the presence of bubbles influence the momentum balance of the liquid. Two-fluid models that account for this phenomenon are referred as two-way coupled models to differentiate them form those in which the exchange of momentum is allowed only from the liquid phase to the disperse phase, which are often called one-way coupled models.

2.5 Turbulence modeling

The blended k-ω turbulence model developed by Menter[20] was used to constitute $\mathbf{T}_c^{Re}$. This model uses a blending function to behave as the k-ω or k-ϵ turbulence model close and away from walls, respectively. In this manner it is possible to take advantage of the strengths of both of these models. Namely,the k-ω model does not require wall damping functions and uses simple Dirichlet boundary conditions and the k-ϵ model does not exhibit sensitivity to the level of free-stream turbulence. Using indicial notation, the balance of turbulent kinetic energy, k, and the turbulent specific dissipation rate, ω, are,[20,21]

$$\alpha_c \frac{\partial k}{\partial t} + \alpha_c \left(u_{cj} - \sigma_k \frac{\partial \nu_t}{\partial x_j} - \sigma_k \frac{\nu_t}{\alpha_c}\frac{\partial \alpha_c}{\partial x_j}\right)\frac{\partial k}{\partial x_j} - \frac{\alpha_c}{R_k}\nabla^2 k - \alpha_c \tau_{ij}\frac{\partial u_{cj}}{\partial x_j} + \alpha_c \beta^* \omega k - \alpha_c \Phi_k = 0 \tag{21}$$

$$\alpha_c \frac{\partial \omega}{\partial t} + \alpha_c \left(u_{cj} - \sigma_\omega \frac{\partial \nu_t}{\partial x_j} - \sigma_\omega \frac{\nu_t}{\alpha_c} \frac{\partial \alpha_c}{\partial x_j} \right) \frac{\partial \omega}{\partial x_j} - \frac{\alpha_c}{R_\omega} \nabla^2 \omega - \alpha_c \gamma \frac{\omega}{k} \tau_{ij} \frac{\partial u_{cj}}{\partial x_j} + \alpha_c \beta \omega^2 + \\ +2(1-F_1)\alpha_c \sigma_{\omega 2} \frac{1}{\omega} \frac{\partial k}{\partial x_j} \frac{\partial \omega}{\partial x_j} - \alpha_c \Phi_\omega = 0 \quad (22)$$

where σ_k, σ_ω, β, β^* and γ are model coefficients and the effective Reynolds numbers, $R_k = 1/(1/Re + \sigma_k \nu_t)$ and $R_\omega = 1/(1/Re + \sigma_\omega \nu_t)$ are defined using the Reynolds number, Re, and the kinematic turbulent viscosity, ν_t. We have adapted the single-phase model for bubbly flows following the work of Lahey.[22] The original single-phase terms are now weighted by the volume fraction of the continuous phase, α_c, as expected for an ensemble-average derivation of the equations. The sources of bubble-induced turbulent kinetic energy and bubble-induced turbulent specific dissipation rate are modeled as,[22]

$$\Phi_k = C_p \sum_{g=1}^{G} \alpha_g \frac{v_{rg}^3}{D_g} \quad (23)$$

where v_{rg} is the absolute value of the local relative velocity for bubbles of diameter D_g and,

$$\Phi_\omega = \frac{\beta}{\beta^*} \frac{\omega}{k} \Phi_k, \quad (24)$$

where $C_p = 0.25$ for potential flow around a sphere.[23] The turbulent viscosity is modeled as,

$$\nu_t = \frac{k}{\omega} + 0.6 \sum_{g=1}^{G} \alpha_g D_g v_{rg}. \quad (25)$$

The first and second terms in equation (25) are the standard single-phase eddy viscosity and the bubble-induced turbulent viscosity, originally derived by Sato et al,[24] respectively.

Although Lahey[22] provides a k-ϵ bubbly flow model, the derivation of its k-ω counterpart is straightforward because the change of variables,

$$\epsilon = \beta^* \omega k \quad (26)$$

makes it possible to derive an equation for ω given one for ϵ.[25] In fact, this change of variables was used by Menter[20] to derive the value of the coefficients of the blended model as,

$$s = F_1 s_1 + (1 - F_1) s_2$$

where s_1 and s_2 are the k-ω model and the transformed k-ϵ model coefficients, respectively. These coefficients can be found elsewhere.[20,21] The blending function, F_1, was designed to be unity in the sublayer and logarithmic regions of boundary layers and gradually switches to zero in the wake region,

$$F_1 = \tanh\left(arg_1^4\right) \quad (27)$$

where,

$$arg_1 = \min\left[\max\left(\frac{k^{1/2}}{0.09\omega\delta};\frac{500\nu}{\delta^2\omega}\right);\frac{4\sigma_{\omega 2}k}{CD_{k\omega}\delta^2}\right], \tag{28}$$

where δ is the distance to the wall and $CD_{k\omega}$ is the positive portion of the cross-diffusion term in equation (22),

$$CD_{k\omega} = \max\left(2\sigma_{\omega 2}\frac{1}{\omega}\frac{\partial k}{\partial x_j}\frac{\partial \omega}{\partial x_j};10^{-20}\right) \tag{29}$$

As mentioned above we choose the same set of coefficients for the turbulent model as Menter,[20] with the exception of β^*, for which we adopt,[25]

$$\beta^* = 0.09 f_{\beta^*} \tag{30}$$

with,

$$f_{\beta^*} = \begin{cases} 1, & \chi_k \le 0 \\ \frac{1+680\chi_k^2}{1+400\chi_k^2} & \chi_k > 0 \end{cases} \tag{31}$$

and,

$$\chi_k = \frac{1}{\omega^3}\frac{\partial k}{\partial x_j}\frac{\partial \omega}{\partial x_j} \tag{32}$$

As will be seen below the adoption of equation (30) greatly improves the agreement between the measured turbulent dissipation in single-phase jets and the predictions of the model. This finding is in agreement with the work of Wilcox,[25] who justified the introduction of equation (30) arguing that it greatly improves the agreement with experimental data for free shear flows while maintaining the good agreement of the original k-ω model with data close to the wall.

We finish our discussion of the two-phase turbulence model by stressing that all its components have been successfully tested by other researchers. Moreover, the blended k-ω model has been widely used in naval hydrodynamics applications.[5,26] The bubbly k-ϵ model has been used to model a wide variety of bubbly conduit flows[22,27,28] and Wilcox[25] strongly recommends the adoption of equation (30).

2.6 Model for the interfacial force

The fluctuating interfacial force density is modeled in the usual way,[17,18,22]

$$\mathbf{M}'_g \cong \mathbf{M}_g^D + \mathbf{M}_g^{TD} + \mathbf{M}_g^{VM} + \mathbf{M}_g^L + \mathbf{M}_g^W \tag{33}$$

where these forces are, respectively, those due to drag (D), turbulent dispersion (TD), virtual mass (VM), lift (L) and wall-induced (W).

The virtual mass force accounts for the effect of acceleration of the liquid displaced by the bubbles, and can be modeled as

$$\mathbf{M}_g^{VM} = \alpha_g\rho_c C_{VM}\left[\left(\frac{\partial \mathbf{u}_c}{\partial t} + \mathbf{u}_c\cdot\nabla\mathbf{u}_c\right) - \left(\frac{\partial \mathbf{u}_g}{\partial t} + \mathbf{u}_g\cdot\nabla\mathbf{u}_g\right)\right], \tag{34}$$

where the virtual volume coefficient, C_{VM}, is 0.5 for the dilute potential flow of spherical bubbles.

The drag force may be expressed as,

$$\mathbf{M}_g^D = -\alpha_g \rho_c C_D \frac{3}{8} \frac{|\mathbf{u}_r|}{D_g/2} \mathbf{u}_r \tag{35}$$

where the drag coefficient C_D is defined by Tomiyama,[29] with a void fraction correction based on that of Ishii[30] to include interaction between the bubbles. For deformed bubbles in contaminated water, the expression for C_D is,

$$C_D = \frac{1}{\alpha_l} \max\left[\frac{24}{Re_D}\left(1 + 0.15\, Re_D^{0.687}\right), \frac{8}{3}\frac{Eo}{Eo+4}\right], \tag{36}$$

Here, Re_D is the bubble Reynolds number based on the bubble diameter, D_g, the relative velocity, $\mathbf{u}_r$, and the Eötvös number, Eo, is defined by:

$$Eo = \frac{g(\rho_l - \rho_g) D_g^2}{\sigma}\ , \tag{37}$$

This non-dimensional number represents the relative importance of buoyancy forces and surface tension, and has been included to take into account the increased drag observed in non-spherical bubbles.

The lift force on a sphere in potential inviscid flow can be expressed as,[31]

$$\mathbf{M}_g^L = -\alpha_g \rho_c C_L\, \mathbf{u}_r \times (\nabla \times \mathbf{u}_c)\ . \tag{38}$$

where C_L = 0.5 for inviscid flows. However, for ship flows the value $C_L = 0.1$ is typically used.[8]

The turbulent dispersion force is modeled as:[8]

$$\mathbf{M}_g^{TD} = -\,\alpha_g^\eta\, \rho_c\, C_{TD} C_D \frac{3}{8} \frac{|\mathbf{u}_r^\eta|}{R_b} \nu_t \frac{\nabla \alpha_g^\eta}{\alpha_g^\eta}\ , \tag{39}$$

where the turbulent dispersion coefficient C_{TD} is defined by

$$C_{TD} = Sc_b^{-1} = \frac{\nu_b}{\nu_t}\,, \tag{40}$$

where $Sc_b = 0.833$ is the bubble Schmidt number, which relates the turbulent diffusivity ν_t of a passive scalar to the bubble diffusivity ν_b. This model has been validated against grid decaying turbulence[32] and jets.[33] Moreover, it rests on a sound theoretical basis, as it is derived from the Boltzmann transport equation for the bubble probability density function.[34,35]

The wall force is decomposed into its tangential and normal parts,

$$\mathbf{M}_g^W = \mathbf{M}_g^{Wt} + \mathbf{M}_g^{Wn} \tag{41}$$

The tangential force density, $\mathbf{M}_g^{Wt}$, is a correction to be added to the bulk drag force density due to the presence of solid walls. We define this *wall drag* force density as:[36,37]

$$\mathbf{M}_g^{Wt} = -\,\alpha_g\,\rho_c\,\frac{3}{4}\frac{\nu_c}{R_b}\frac{(\mathbf{u}_g-\mathbf{u}_c)\cdot(\mathbf{I}-\mathbf{nn})}{\delta}, \tag{42}$$

where δ is the gap between the bubble and the wall and the tensor $(\mathbf{I}-\mathbf{nn})$ is used to pick the velocity tangential to the wall. ($\mathbf{I}$ and $\mathbf{n}$ are the identity matrix and the exterior normal to the wall). Moraga et al[17] assessed this model using the experimental data of Tsao and Koch[38] who measured the drag of a bubble sliding along a wall.

For the normal force, $\mathbf{M}_g^{Wn}$, the bubble and its surrounding liquid is modeled as a damped oscillator.[11] The elastic force is due to the surface tension that resists the deformation of the bubble and the virtual mass plays the role of the inertia. In this simple model, the viscous force keeps the gas normal velocities under control during numerical iterations. The resultant linear model for the normal force density, elastic and viscous, is,

$$\begin{aligned}\mathbf{M}_g^{Wn} = \quad & -\left[\frac{C_{WE}\sigma}{C_{VM}\rho_c V_b}\left(R_b^*-R_b\right)+\right. \\ & \left. C_{WV}\sqrt{\frac{C_{WE}\sigma}{C_{VM}\rho_c V_b}}\left(\mathbf{u}_g\cdot\mathbf{n}\right)\right]\alpha_g\rho_c\mathbf{n}\end{aligned} \tag{43}$$

where the corrected bubble radius, R_b^*, is given by,

$$R_b^* = R_b\left(1-e^{-\left(\frac{d_w}{R_b}\right)^3-\frac{d_w}{R_b}}\right) \tag{44}$$

and the recommended values for the elastic and viscous coefficients are

$$C_{WE}=2.3\,; \qquad C_{WV}=5. \tag{45}$$

The normal wall-induced force model used here is robust enough to handle inclined and horizontal walls. In contrast the models of Antal et al[39] and Moraga et al[17] may underestimate the force on an inclined wall.[38] The latter is the only one that accounts explicitly for the effect of the bubble Weber number and is based on an analytic solution[40] without any adjustable coefficients. Although there is empiricism in the wall-force model used, it is not expected to adversely impact the quality of the results as all comparisons of bubble void fractions with experimental data are done far enough away from walls as to ensure that wall forces are unimportant.

2.7 Surface capturing algorithm

A single-phase level set method was used to capture the interface position.[5,26] Unlike the two-phase level set, the one-phase level set technique does not solve the Navier-Stokes equations in the air, neglects viscous stresses at the interface and keeps the sharp discontinuity of the density at the interface. Moreover, the one-phase level set technique has been found to be much less prone to the instabilities of high density ratio flows than the two-phase level set technique and is capable of accurately predicting flows dominated by the liquid inertia.[5,41]

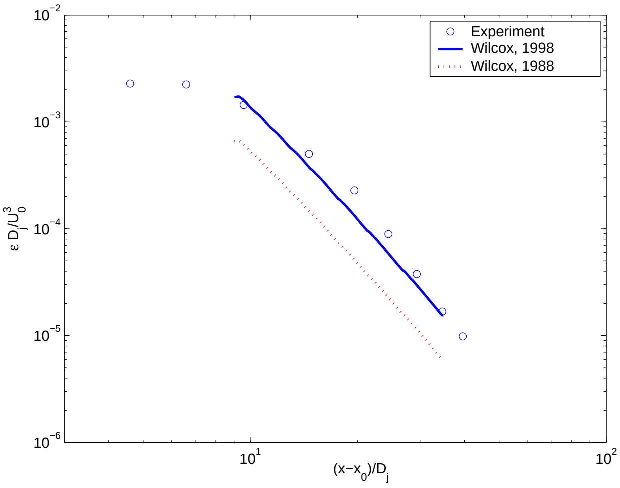

Figure 1: Dimensionless turbulent dissipation along the centerline of a self-similar jet.

3 SIMULATIONS

3.1 Validation of the Bubble Break-up Model

Given the importance of accurately computing the turbulence dissipation, ϵ, for the prediction of bubble breakup, which, in turn, has to be accurately modeled to predict the bubble size distributions and void fraction distributions, it is desirable to simulate a simple canonical flow where the predictions of the turbulence dissipation and the breakup model can be assessed. For this purpose we present simulations of an upward turbulent polydisperse bubbly jet characterized by Martinez-Bazan et al.[10,14] The single-phase Reynolds number based on the jet diameter and the inlet velocity was $Re = 25,500$. Since great care was taken by Martinez-Bazan et al[10,14] to ensure that the measurements were made in the self-similar region of the jet, and since the void fractions were small enough to ensure a one-way coupled flow, there was no need to solve for the mean liquid velocities, and k and ω in a three-dimensional computational domain. Instead the self-similar solution of the turbulent single phase jet,[25] was copied into a 3D grid which was used to calculate the evolution of the disperse phase. Figure-1 shows the dissipation profiles obtained when using $f_{\beta^*} = 1$ as in the original k-ω model[42] and f_{β^*} as given by equation (31).[25] The virtual origin is located at $x_0 = 5.4D_j$ where D_j is the jet diameter.

Unlike most models for binary breakup, the daughter bubbles are not assumed to be of the same size. As a consequence, special care has to be given to the discretization of the bubble diameters in a computer implementation of the model, to ensure that the breakup of small bubbles is properly captured. We have found that a logarithmic distribution of bubbles sizes $D_g; g = 1, 2, ..G$ is preferable over an equally spaced distribution as it helps ensure that the ratio $\Delta D_g/D_g$ is small even for small D_g, where ΔD_g is the width of the bin centered at D_g. For logarithmic spacing we found no considerable difference in the simulations results for $G = 15, 30$ or 60. Figure-2 shows the downstream evolution of the number of bubbles belonging to the largest class N_G, which is scaled by the ratio of the local axial velocity, U, and

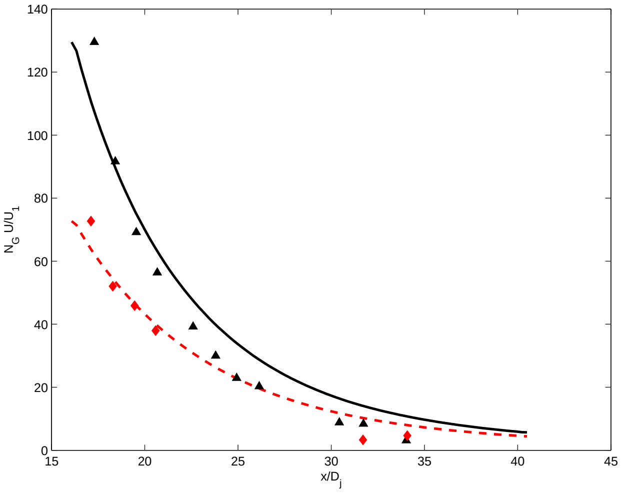

Figure 2: Downstream evolution of the number of bubbles belonging to the largest class N_G. Symbols: Experimental data. Lines: Simulations. Red and black correspond to case 3a and 3b,[10] respectively

the axial velocity at the first measurement station, U_1. This scaling is necessary to present the data in the same manner than in Figure 13 of the work by Martinez Bazan et al [10,]. Figure-3 shows the downstream evolution of the total bubble flux, $N_t U/L_w$. Due to the very high liquid velocities the bubble velocities can be approximated by the liquid velocity U. The constant L_w is the width of the region used to collect statistics.[10]

3.2 Simulation of a breaking bow wave

We present in this section simulations of a steady breaking bow wave characterized by Waniewski et al.[2,43] Our interest in this experiment is based on the fact that to the best of our knowledge it is the only published work that reports measurements of the air entrainment and enough information on the flow is given to unambiguously reproduce it in a computer simulation. A top view of the channel where the breaking wave was produced can be seen in Figure-4. A flat vertical plate was mounted forming an angle of 26° with the incoming flow. The depth of the channel far away from the wall was $d = 7.89$cm. The leading edge of the plate was mounted 12 cm away from the closest flume wall. Due to the finite length of the plate we choose to simulate the flow on both sides of it.

The computational domain extended from $x/d = -5$ to $x/d = 40$. The grid had approximately 1,204,000 cells with approximately 680,000 cells belonging to chimera overset grids concentrated in the breaking region. Although we did not conduct grid convergence studies, we point out that our grid was designed as to have similar resolution in the breaking region to the finest grid used by Broglia et al,[41] who also simulated the same experiment using a one-phase level set but neglected the bubbles entrained by the breaking wave. These researchers conducted grid convergence studies and concluded that they had sufficient resolution. A uniform velocity field with an upstream value $U = 2.48$ m/s, zero pressure field and a flat free surface were used

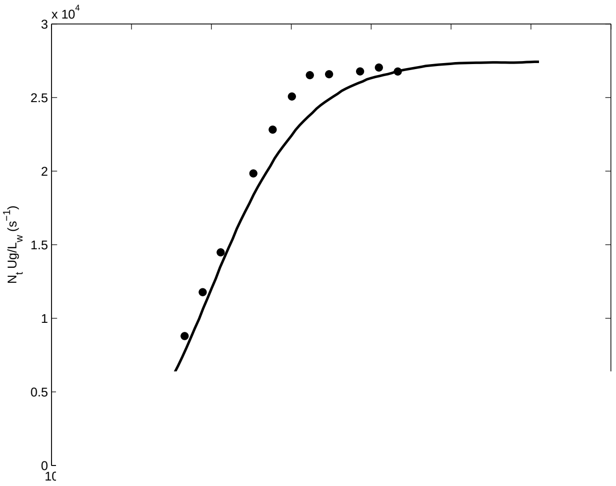

Figure 3: Downs

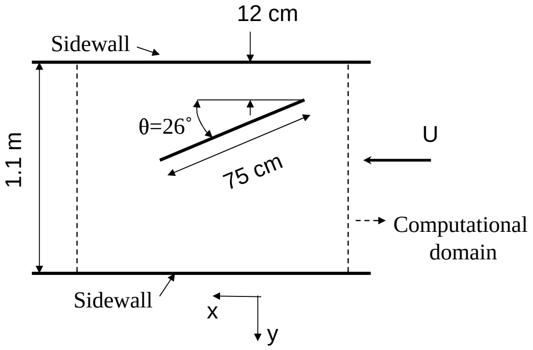

Figure 4: Top view of the test section.[2,43]

as the initial conditions to obtain a steady-state solution for the problem without bubbles. This steady state-solution was used as the initial condition for the simulation of the bubbly flow. The bubbly flow simulations are conducted for approximately 0.08 s of real time. During this interval bubbles moving at the free stream velocity move approximately 20 cm, which gives sufficient time for the bubbles to travel across the region having air entrainment measurements. Since all the measurements conducted by Waniewski et al[2] correspond to steady-state conditions, we present results corresponding to the end of our simulations.

A uniform free stream velocity $U = 2.48$ m/s was imposed at the inflow plane, $x/d = -5$, while zero pressure and velocity gradients were imposed at the outflow. No-slip boundary conditions were used for all vertical walls. However, using a slip boundary condition at the bottom wall, Broglia et al[41] found satisfactory agreement with experimental data for the contact line, the width and angle of the plunging jet and the jet impact velocity. Thus, we also chose not to resolve the boundary layer at the bottom wall. This obviously presents the great advantage of reducing the size of the final grid. Our primary interest is in the measurements of air entrainment, which are expected to depend on the just mentioned width and angle of the plunging liquid jet and the jet impact velocity (i.e., these parameters define the Reynolds and Froude number which together with the jet angle determine the amount of ingested air[3]). Thus we believe that neglecting the bottom boundary layer introduces a negligible effect on the air entrainment features of the flow. Indeed the main consequence of not resolving the bottom boundary layer is a shift of the position of the jet impact line which can easily be corrected for with a translation offset. This shift is of approximately $\Delta x =$ -13.8 cm and $\Delta y =$ 15 cm, where the negative sign indicates that in the simulations the origin of the jet impact line occurs at a value of x lower than in the experiment. We observe that despite of this shift it is still possible to compare the position of the air entrainment region between experiment and simulation, because this shift is applied to the whole flow. That is the position of the interface between continuous fluids is displaced along with that of the air entrainment region.

The following distribution of bubble radii was used: $D_g/2$= 0.080, 0.100, 0.126, 0.159, 0.120, 0.251, 0.315, 0.397, 0.499, 0.627, 0.787, 1.000, 1.250, 1.500, 1.750, 2.000, 2.5000, 3.0000, 3.500 and 4.000 mm. All radii are given in mm. The upper boundary of the size distribution was chosen based on the fact that Waniewski et al[2] detected bubbles of chordal lengths of 8 mm and higher, although their relative abundance decreased strongly with depth. We have shown previously that 20 bubble sizes is a sufficient number to properly model the bubble breakup provided that logarithmic spacing is used for small bubbles. We specify the source intensity using the acoustic phase bubble size distribution measured by Deane & Stokes[1] (i.e., $\alpha = -3/2, \beta = -10, 3$). Although Waniewski et al[2] conducted measurements of bubble size distribution the characteristic width of each bubble class was $\Delta D_g =$ 1 mm. We know from the results in section 3.1 that this is insufficient to properly resolve the dynamics of bubble breakup. Moreover, Waniewski et al[2] make no distinction between the acoustic and the quiescent regions. As it was mentioned above, we think that the bubble source distribution specified has to correspond to the acoustic phase, as the phenomena in the quiescent phase are modeled by our two-fluid model.

Figure-5 shows the simulated contact line and that measured experimentally for the closest experimental conditions. Unfortunately, Waniewski et al[2,43] did not measure the contact line for exactly the same conditions as used to measure air entrainment, but runs 4l, 5l and 6l in the work by Waniewski et al[43] are for similar conditions. These runs correspond to free stream velocities, U =2.61, 2.40, 2.46 m/s and drafts, $d =$ 6.45, 7.62 and 9.32 cm, respectively. In contrast our simulations correspond to air entrainment runs with U =2.48 m/s and $d = 7.89$ cm. Thus, we expect our results to fall in between the experimental data. This is the case for most of the range of the horizontal distance to the leading edge, r. Close to the leading edge we tend to underestimate the height of contact line. Broglia et al[41] also tend to underestimate this height and speculated that the leading edge region is more sensitive to viscous effects. Our runs conducted without bubble injection show virtually the same contact line as for runs with injection. This is not surprising given that bubbles are being introduced far away from the

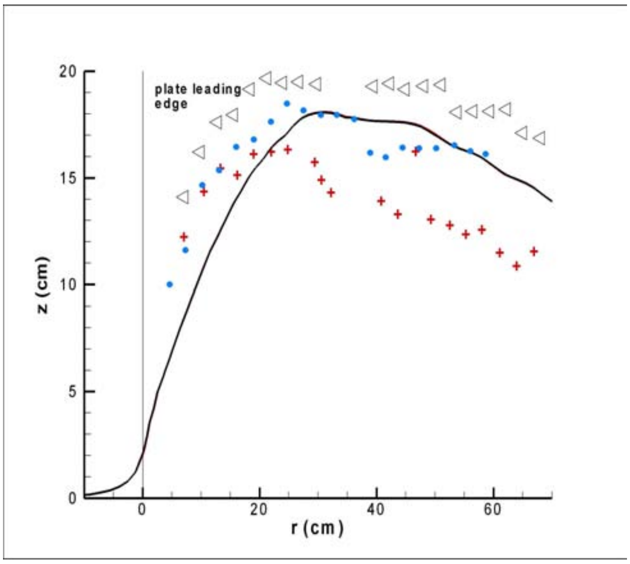

Figure 5: Comparison of simulated and measured contact lines (symbols). Line: simulations, U =2.48 m/s, d = 7.89 cm. Circles: Run 4l, U =2.61 m/s, d = 6.45 cm. Plus: Run 5l, U =2.40 m/s, d = 7.62 cm. Triangles: Run 6l, U =2.46 m/s, d = 9.32 cm.

contact line.

Figures-6 a,b and c show cuts of the wave at planes x = 73.4, 81.0 and 91.2 cm. The shape of the wave is very similar to that of the experiments (See Figure 11 in the work by Waniewski et al.[43] For the first impact, at x = 73.4 cm the jet width is approximately 2.5 cm and the jet impingement angle is 58°, in agreement with the experimental data.[43] The impact velocities in the simulations range between 2.0 and 2.2 m/s depending on the position along the jet where its measured. These numbers compare favorably with the value 2.3 m/s measured by Waniewski et al.[43] In these figures the calculated void fraction contours can also be seen in continuous color, while the blue line indicates the top 1% void fraction from the experimental data.[43] It must be mentioned that because the free surface oscillates during the measurements it was not possible to measure the void fraction at locations above z =-1 cm without the free surface dipping below the measuring probe or the probe entraining air.[2] Thus, in agreement with the simulations, the region of higher void fraction is above the 1% void fraction line from the experimental measurements. Only a distance of a few centimeters in the vertical direction separates the 1% void fraction line of experiments and simulations, while in the horizontal direction there is excellent agreement. Given the simplicity of our air ingestion model and the fact that it has just one adjustable constant, S_0 in equation 2, this agreement is surprisingly good. All other model parameters were taken from the work of other researchers. We believe that part of the discrepancy between the void distribution of the simulation and the experiment is due to the fact that in the simulations the same source intensity is used for all points at which bubbles are ingested, while that is probably not the case for the experiments. Nevertheless, we point out that a shift of dimensions comparable to the width of the plunging bow wave is negligible in the length scales of a ship and ship simulations are the main intended purpose of our model. We also point out that this level of accuracy is a considerable improvement over previous work in which the source location was specified by a human expert[6–8] after examining the solution for the problem without bubble ingestion. The main drawback of the injection algorithm is that a region of void fractions of about 1 or 2% can be observed in the top region of the plunging jet ($z > 5$ cm), where a single phase jet was expected. However, this void fraction is small enough to have little impact on the final results for the void fraction downstream of the breaking wave. Moreover, we point out that in the region of air entrainment the liquid is decelerating in the vertical direction, while in the top portion of the jet it is accelerating. Thus, we believe that the injection at the top of the jet could be avoided if not only the local velocity is used for the injection criterion but also the local acceleration. Future versions of the model will aim at including the sign of the acceleration.

Maximum values of the dissipation in the region of jet impact are approximately of $\epsilon = 7$ m^2/s^3. Unfortunately Waniewski et al[2] did not measure dissipation, so we compare with the dissipation estimates and measurements of Deane & Stokes[1] and Lowen & Meville,[44] respectively. In both works the cited value of the dissipation is $\epsilon = 13$ m^2/s^3. Given the differences in flow configuration between the breaking waves we simulate and those of Deane & Stokes[1] and Lowen & Meville[44] we believe this level of agreement is quite satisfactory.

3.3 Simulation of the bubbly flow around a naval surface ship

In this section we present simulations of the bubbly flow around the unappended naval combatant, DTMB 5415, in steady forward motion at a velocity $U = 3.5$ m/s, Reynolds number, $Re = UL/\nu = 1.57 \times 10^7$ and Froude number $Fr = U/\sqrt{gL} = 0.35$, where $L = 142$ m is the ship length. The values of the Reynolds and Froude number were chosen so as to generate a strong breaking bow wave with a moderate computational cost. The grid consists of approximately 1,600,000 cells with approximately 650,000 cells concentrated in chimera overset grids at the bow wave region. This level of resolution is insufficient to capture all the details of the flow particularly at the transom and the bow wave where 3 levels of nesting of chimera overset grids and unsteady simulations are necessary to be able to make quantitative comparisons with experiments at tow tank conditions.[26] Given that there are no void fraction measurements around ship hulls in the open literature, the main purpose of this simulation was to evaluate the qualitative trends. In particular we want to asses whether our model can identify the locations of air ingestion. We believe that the spatial resolution adopted is sufficient for this purpose. For similar reasons no efforts were made to adjust the source intensity to produce a predetermined void fraction. Similarly only 6 different bubble sizes were considered ($D_g = 100,$ 126, 158, 199, 250 and 314 μm) and the bubble-induced source of turbulent kinetic energy was set to zero, $\Phi_k = 0$.

Figure-7 shows a perspective of the ship hull and the near-hull portion of the free surface. Dark blue is used to indicate the portion of the free surface where bubbles can be observed. Notice the qualitative resemblance with the flows at sea. The bubbles were given approximately 80 s to travel along the computational domain. Figure-8 shows a bottom view. The hull and free surface are shown in the same colors than in the previous figure. The top portion of the figure shows isosurfaces of total void fraction at and below the free surface (Dark blue), while the bottom portion shows the void fraction contours at approximately 200 μ from the hull. The pink squares indicate the points where bubbles are injected. In agreement with visual observations at sea, both below and above the free surface, the mode predicts that bubbles are injected at the impact line of the breaking bow wave, at the contact line behind the bow wave and at the transom stern. To the best of our knowledge this is the first time that a numerical simulation predicts that there is air entrainment at the transom stern and below the contact line behind the breaking bow wave.

4 CONCLUSIONS

We have developed a 3-D, two-fluid model which is capable of simulating air entrainment flows. A subgrid model was developed to determine the location of the bubble source due to air ingestion. This model is based in the simple observation that the non-linear dependence of the terminal velocity with bubble diameter originates at a region of high void fraction in and around the air entrainment region. Combined with a model for bubble breakup, and a bubbly k-ω model, the subgrid model can reproduce experimental results for a steady breaking bow wave. Even though the source intensity is adjusted to match experimental data, the new model represents considerable improvement in the field of bubbly flow simulations for naval hydrodynamics as it eliminates the need to estimate the location of the air entrainment region. Moreover, this model opens new possibilities. For example, it makes it possible to conduct parametric studies on the impact of the void fraction on many flows of interest. This is particularly important for flows in which high void fraction regions are known to occur (10 or 20 % are typical values) and are currently modeled as single-phase flows by practically all the design tools available to naval architects. The model also diminish the uncertainties related to bubbly flow simulations around naval ship hulls aimed at determining the acoustic signature of the bubbly wake.

Comparison with the experimental data of Wanieski et al was favorable, with the vertical location of the predicted 1% void fraction line approximately just half a jet width away from that of the measurements. The model was also applied to simulations of naval combatant DTMB5415, where it qualitatively identified the right location for the air entrainment regions.

It is possible that using other flow parameters, more sophisticate versions of an injection algorithm can be applied. For example it has been suggested that the air entrainment region correlates with high turbulence intensity and high turbulent dissipation. However, the increase of these quantities is a direct consequence of the bubbles and consequently it is difficult to detect in the initial single phase flow. For this reason we believe that a model based on the averages liquid velocities is more robust. Once bubbles are present in the flow the turbulent kinetic energy and dissipation can be used to introduce improvements.

5 ACKNOWLEDGEMENTS

This work was supported in part by a grant of computer time from the DOD High Performance Computing Modernization Program at US Army Engineering and Research Development Center (ERDC), Army Research Laboratory (ARL) and Artic Region Supercomputer Center (ARSC).

REFERENCES

[1] B. D. Deane and M. D. Stokes. Scale dependence of bubble creation mechanisms in breaking waves. Nature, **418**, 839–844 (2002).

[2] T. A. Waniewski, C. E. Brennen, and F. Raichlen. Measurement of air entrainment by bow waves. J. Fluids Eng., **123**, 57–63 (2001).

[3] H. Chanson. *Air Bubble Entrainment in Free-Surface Turbulent Shear Flows*. Academic Press, (1996).

[4] A. Iafrati, E. F. Campana, R. Gomez Ledesma, K. T. Kiger, and J. H. Duncan. Air entrainment induced by the impact of a planar translating jet on a flat free surface. Proc. 25th Symposium on Naval Hydrodynamics, **3**, 84 (2004).

[5] P. M. Carrica, R. V. Wilson, and F. Stern. An unsteady single-phase level set method for viscous free surface flows, IIHR technical report 444, april 2005. Iowa Institute for Hydraulic Research. The University of Iowa, Iowa, USA., (2005).

[6] F. J. Moraga, D. A. Drew, and R. T. Lahey, Jr. The modeling and simulation of bubbly flows around surface ships. In *Proceedings of 3rd International Symposium on Two-Phase Flow Modeling and Experimentation*, Pisa, Italy, (September 2004).

[7] F. J. Moraga, D. A. Drew, and R. T. Lahey, Jr. The modeling of bubbly flows around naval surface ships at high reynolds numbers. In *Proceedings of* 2^{nd} *MIT Conference on Computational Fluid and Solid Mechanics*, (June 2003).

[8] P. M. Carrica, D. A. Drew, and R. T. Lahey, Jr. A polydisperse model for bubbly two-phase flow around a surface ship. *Int. J. Multiphase Flow*, **25**, 257–305 (1999).

[9] A. Tomiyama, K. Sakoda, K. Hayashi, A. Sou, N. Shimada, and S. Hosokawa. Modeling and hybrid simulation of bubbly flow. In Japan-US seminar on two-phase flow dynamics., volume 1, pages 1–15, Nagahama, Japan, (2004).

[10] C. Martinez-Bazan, J.L. Montañes, and J. C. Lasheras. On the breakup of an air bubble injected into a fully developed turbulent flow. part 1. breakup frequency. J. Fluid Mech., **401**, 157–182 (1999a).

[11] A. E. Larreteguy, D. A. Drew, and R. T. Lahey, Jr. A center-averaged two-fluid model for wall-bounded bubbly flows. In *2002 Joint US ASME/ European Fluids Engineering Division. Summer Meeting. July 14-18*, Montreal. Canada, (2002).

[12] C. Clanet and J. C. Lasheras. Depth of penetration of bubbles entrained by a plunging water jet. Physics of Fluids, **9**, 1864–1866 (1997).

[13] R. Clift, J. R. Grace, and M. E. Weber. *Bubbles, drops and particles.* Academic Press, (1978).

[14] C. Martinez-Bazan, J. L. Montañes, and J. C. Lasheras. On the breakup of an air bubble injected into a fully developed turbulent flow. part 2. size pdf of the resulting daughter bubbles. J. Fluid Mech., **401**, 183–207 (1999b).

[15] C. Martinez-Bazan, J.L. Montañes, and J. C. Lasheras. Statistical description of the bubble cloud resulting from the injection of air into a turbulent water jet. Int. J. Multiphase Flow, **28**, 597–615 (2002).

[16] G. K. Batchelor. The theory of homogeneous turbulence. Cambridge University Press, (1956).

[17] F. J. Moraga, A. E. Larreteguy, D. A. Drew, and Jr. Lahey, R. T. A center-averaged two-fluid model for wall-bounded bubbly flows. Computers & Fluids, (2005). In press. Corrected proof is available online (doi:10.1016/j.compfluid.2005.02.002).

[18] D.A. Drew and S.L. Passman. *Theory of multicomponent fluids*, volume 135 of *App. Math. Sci.* Springer, (1998).

[19] A. E. Larreteguy, P. M. Carrica, D. A. Drew, and R. T. Lahey, Jr. *CFDShipM: Multiphase Code for Ship Hydrodynamics. Version 2.24 Users manual.*, (1999).

[20] F. R. Menter. Two-equation eddy viscosity turbulence models for engineering applications. AIAA Journal, **32**(8), 1598–1605 (1994).

[21] E. G. Paterson, R. V. Wilson, and F. Stern. General-purpose parallel unsteady rans ship hydrodynamics code: Cfdship-iowa. IIHR report no. 432. Technical report, Iowa Institute for Hydraulic Research. The University of Iowa, Iowa, USA., (2003).

[22] R.T. Lahey, Jr. The simulation of multidimansional multiphase flows. Nuclear Engineering and Design., **235**, 1043–1060 (2005).

[23] G. Arnold, D. A. Drew, and R.T. Lahey, Jr. Derivation of constitutive equations for interfacial force and reynolds stress fo a suspension of spheres using ensemble averaging. Chem. Eng. Commu., **86**, 43–54 (1989).

[24] Y. Sato, M. Sadatomi, and Sekoguchi K. Momentum and heat transfer in two-phase bubble flow-i. *Int. J. Multiphase Flow*, **7**, 167–177 (1981).

[25] D. C. Wilcox. *Turbulence modeling for CFD.* DCW Industries, California, (1998).

[26] P. M. Carrica, R. V. Wilson, and F. Stern. Unsteady rans simulation of the ship forward speed diffraction problem. *Computers & Fluids.* In Press. Corrected proof available online (doi:10.1016/j.compfluid.2005.08.001).

[27] A. A. Troshko and Hassan Y. A. A two-equation turbulence model of turbulent bubbly flows. Int. J. Multiphase Flow, **27**(11), 1965–2000 (2001).

[28] M. S. Politano, P. M. Carrica, and Converti J. A model for turbulent polydisperse two-phase flow in vertical channels. Int. J. of Multiphase Flow, **29**(7), 1153–1182 (2003).

[29] A. Tomiyama. Struggles with computational bubble dynamics. In *Third Int. Conf. on Multiphase Flows, ICMF98*, Lyon, France, (1998).

[30] M. Ishii. Two-fluid model for two-phase flow. In *2nd Int. Workshop on Two-Phase Flow Fundamentals*, Rensselaer Polytechnic Institute, Troy, NY, (1987).

[31] T. R. Auton. The lift force on a spherical body in a rotational flow. *J. Fluid Mechanics*, **183**, 199–213 (1987).

[32] F. J. Moraga, A. E. Larreteguy, D. A. Drew, and R. T. Lahey, Jr. Assessment of turbulent dispersion models for bubbly flows in the low stokes number limit. *Int. J. Multiphase Flow*, **29**(4), 655–673 (2003).

[33] M. Lopez de Bertodano, F. Moraga, D. A. Drew, and Jr. Lahey, R. T. The modeling of lift and dispersion forces in two-fluid model simulations. part-i: Jet flows. In *Proceedings of 8th International Symposium On Gas-Liquid Two-Phase Flows, ASME/JSME Joint Fluids Engineering Division Summer Meeting*, Honolulu, Hawaii, (July 2003).

[34] D. A. Drew. A turbulent dispersion model for particles or bubbles. *J. Eng. Mathematics*, **41**(2-3), 259–274 (2001).

[35] M. Lopez de Bertodano. Two fluid model for two-phase turbulent jet. Nuclear Engineering and Design., **179**, 65–74 (1998).

[36] M. Lopez de Bertodano. *Turbulent Bubbly Two-Phase Flow in a Triangular Duct.* PhD thesis, Rensselaer Polytechnic Institute, Troy, NY, (1992).

[37] R.T. Lahey, Jr., Lopez de Bertodano M., and Jones Jr. O.C. Phase distribution phenomena in complex geometry conduits. *Nuclear Eng. and Design*, **141**, 177–201 (1993).

[38] H-K Tsao and D. Koch. Observations of high reynolds number bubbles interacting with a rigid wall. Phys. Fluids, **9**(1), 44–56 (1997).

[39] S.P. Antal, R. T. Lahey, Jr., and J.E. Flaherty. Analysis of phase distribution in fully developed laminar bubbly two-phase flow. *Int. J. Multiphase Flow*, **17**, 635–652 (1991).

[40] H-K Tsao and D. Koch. Collisions of slightly deformable, high reynolds number bubbles with short-range repulsive forces. *Phys. Fluids*, **6**(8), 2591–2605 (1994).

[41] R. Broglia, A. Di Mascio, and R. Muscari. Numerical simulation of breaking wave around a wedge. Proc. 25th Symposium on Naval Hydrodynamics., **1**, 9 (2004).

[42] D. C. Wilcox. Reassessment of the scale-determining equation for advanced turbulence models. AIAA Journal, **26**(11), 1299–1310 (1988).

[43] T. A. Waniewski, C. E. Brennen, and F. Raichlen. Bow wave dynamics. J. Ship Research, **46**(1), 1–15 (2002).

[44] M. R. Loewen and W. K. Meville. Microwave backscatter and acoustic radiation from breaking waves. J. Fluid Mechanics, **224**, 601–623 (1991).

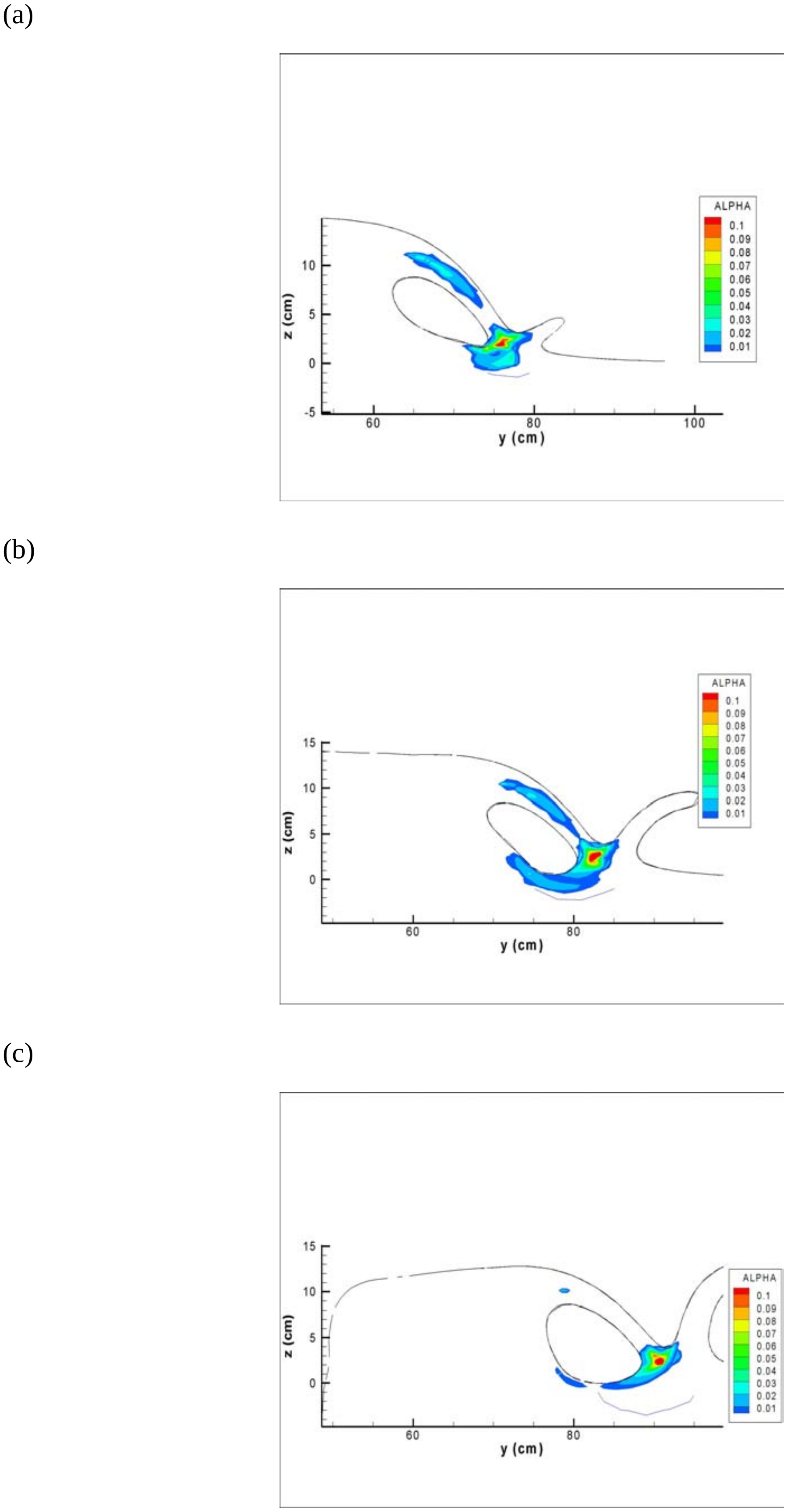

Figure 6: Wave profile (black line) and total void fraction distribution (colored contours) at (a) $x = 73.4$ cm, (b) $x = 81$ cm and (c) $x = 91.2$ cm. The blue line indicates the measured 1% void fraction line from experiments.

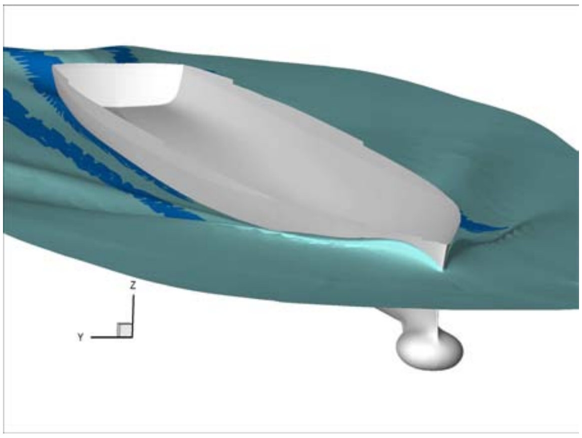

Figure 7: View of the unappended hull of DTMB5415 (gray) and the free surface (grayish blue) with the region of the free surface covered by bubbles indicated in dark blue.

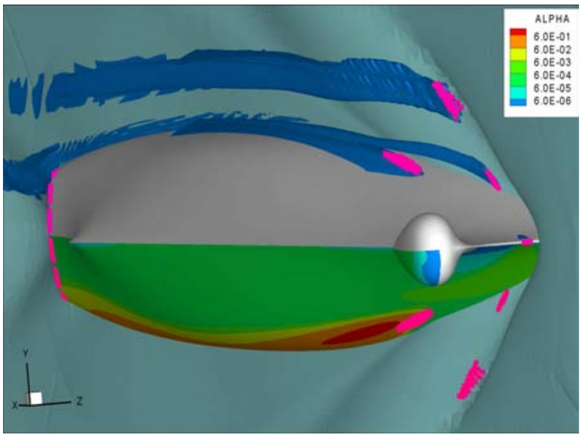

Figure 8: Bottom view of the bubbly flow around the unappended DTMB5415. For details see the text.